

Article

Comparison of Hydrogen Embrittlement Susceptibility of Different Types of Advanced High-Strength Steels

Sangwon Cho ^{1,†}, Geon-Il Kim ^{1,†}, Sang-Jin Ko ¹, Jin-Seok Yoo ¹, Yeon-Seung Jung ², Yun-Ha Yoo ² and Jung-Gu Kim ^{1,*}

¹ School of Advanced Materials Science and Engineering, Sungkyunkwan University (SKKU), Suwon 16419, Korea; jsw2811@gmail.com (S.C.); geonil1027@g.skku.edu (G.-I.K.); tkdwls121@skku.edu (S.-J.K.); wlstjr5619@skku.edu (J.-S.Y.)

² Steel Solution Research Laboratory, POSCO Global R&D Center, Incheon 21985, Korea; ysj799@posco.com (Y.-S.J.); yunha778@posco.com (Y.-H.Y.)

* Correspondence: kimjg@skku.edu; Tel.: +82-31-290-7360

† These authors contributed equally to this study.

Abstract: This study investigated the hydrogen embrittlement (HE) characteristics of advanced high-strength steels (AHSSs). Two different types of AHSSs with a tensile strength of 1.2 GPa were investigated. Slow strain rate tests (SSRTs) were performed under various applied potentials (E_{app}) to identify the mechanism with the greatest effect on the embrittlement of the specimens. The SSRT results revealed that, as the E_{app} increased, the elongation tended to increase, even when a potential exceeding the corrosion potential was applied. Both types of AHSSs exhibited embrittled fracture behavior that was dominated by HE. The fractured SSRT specimens were subjected to a thermal desorption spectroscopy analysis, revealing that diffusible hydrogen was trapped mainly at the grain boundaries and dislocations (i.e., reversible hydrogen-trapping sites). The micro-analysis results revealed that the poor HE resistance of the specimens was attributed to the more reversible hydrogen-trapping sites.

Keywords: advanced high-strength steel; hydrogen embrittlement; hydrogen trapping; thermal desorption spectroscopy



Citation: Cho, S.; Kim, G.-I.; Ko, S.-J.; Yoo, J.-S.; Jung, Y.-S.; Yoo, Y.-H.; Kim, J.-G. Comparison of Hydrogen Embrittlement Susceptibility of Different Types of Advanced High-Strength Steels. *Materials* **2022**, *15*, 3406. <https://doi.org/10.3390/ma15093406>

Academic Editors: Lucjan Śniezek and Jaroslaw Galkiewicz

Received: 15 April 2022

Accepted: 7 May 2022

Published: 9 May 2022

Publisher's Note: MDPI stays neutral with regard to jurisdictional claims in published maps and institutional affiliations.



Copyright: © 2022 by the authors. Licensee MDPI, Basel, Switzerland. This article is an open access article distributed under the terms and conditions of the Creative Commons Attribution (CC BY) license (<https://creativecommons.org/licenses/by/4.0/>).

1. Introduction

The need to reduce environmental harm is a growing global concern. Accordingly, the automotive industry is striving to improve fuel efficiency and reduce carbon dioxide emissions to protect the environment. Globally, the industry is pushing for fuel efficiency improvements via two routes: high-efficiency engines and lightweight body designs [1–3]. A vehicle's body weight accounts for 40% of its fuel efficiency factors; therefore, reducing this weight has the greatest impact on improving fuel efficiency. Generally, a 100-kg reduction in body weight lowers carbon dioxide emissions by 7.5 to 12.5 g/km, significantly enhancing the fuel efficiency. To reduce the weight of cars, manufacturers may use nonferrous materials (e.g., resin, aluminum alloy, and magnesium alloy) [4–8]; specific methods (e.g., the miniaturization of parts); or different types of high-strength steels [9–11]. Although nonferrous materials used in automotive structures such as aluminum alloy and magnesium alloy are lighter than steel, they are also weaker, and their thicknesses must be increased to maintain body stiffness. Additionally, lightweight materials must be used in combination with other materials, such as carbon fiber-reinforced plastic, to maintain the required body stiffness. Therefore, research and development into various types of advanced high-strength steels (AHSSs) are currently underway.

Generally, the mechanical properties of steel are enhanced using methods such as solid solution, grain refinement, or precipitation; however, in the case of AHSS, phase transformation-based methods are also used. Enhancing the mechanical properties of an

AHSS increases its corrosivity and sensitivity to a delayed fracture, i.e., stress–corrosion cracking (SCC) and hydrogen embrittlement (HE), which are the main problems associated with AHSS [12].

Over the past decades, a lot of research on HE in AHSSs has been conducted: effects of the strength, microstructure, and types of defects of AHSSs. V. G. Khanzhin et al. [13,14] studied the influence of precipitate and mechanical properties on HE. According to the studies, the higher density of precipitates in a structure, the lower HE resistance, since the secondary phase particles influence both the stage of initiating hydrogen cracks and the crack growth kinetics to a critical value. Additionally, mechanical properties, their strength and toughness, affects the nucleation of hydrogen cracks, possibility of their propagation, and the kinetics of growth to a critical size.

In AHSS, the delayed fracture phenomenon is caused mainly by HE. Hydrogen inside the steel is preferentially trapped in lattice defects, such as voids, dislocations, and grain boundaries, as well as in various carbides and precipitates [15,16]. Additionally, after entrapment, hydrogen is concentrated in certain areas by stress, leading to the propagation of internal cracks and, eventually, to delayed fractures. However, the exact cause and mechanism of the delayed fracture phenomenon have not been identified to date. This is because, in addition to HE, a delayed fracture can result from the combined effects of other variables, including the stresses acting on the steel, the microstructures, mechanical properties, surface conditions, and internal cracks. Further research is required to determine the exact cause of HE. Therefore, this study uses slow strain rate tests (SSRTs), a microstructural analysis, and a thermal desorption spectroscopy (TDS) analysis to investigate the HE mechanisms of two different types of AHSSs with the tensile strength of 1.2 GPa.

2. Materials and Methods

This study used two different types of AHSSs with a tensile strength of 1.2 GPa. Table 1 provides their chemical compositions. Figure 1 presents the specimens' microstructural images, and Figure 2 shows the mechanical properties obtained by the tensile test. Steel A was comprised of fine grains with complex phases of ferrite, bainite, martensite, and a small fraction of retained austenite, with Ti and/or Nb precipitates for enhancing the tensile strength and ductility. Since this steel was cooled slowly after soaking in the austenite region, its main phases were bainite and martensite. Steel B was also a multiphase AHSS comprising ferrite, bainite, a relatively higher fraction of retained austenite, and a small portion of martensite. Under an applied stress, the phase transformation of the retained austenite increased the ductility of Steel B. As shown in Figure 2c, Steel B showed a uniform strain-hardening rate range, which is evidence of a transformation-induced plasticity effect.

Table 1. Chemical compositions of the advanced high-strength steels for use in automobiles (wt.%).

Component	C	Si	Mn	Cr	Ti	Nb	Fe
Steel A	0.11~0.18	0.4~0.7	2.2~2.7	0.0~0.1	0.01~0.02	0.01~0.02	Bal.
Steel B	0.11~0.18	1.2~1.9	2.4~2.7	0.20~0.45	0.01~0.02	-	Bal.

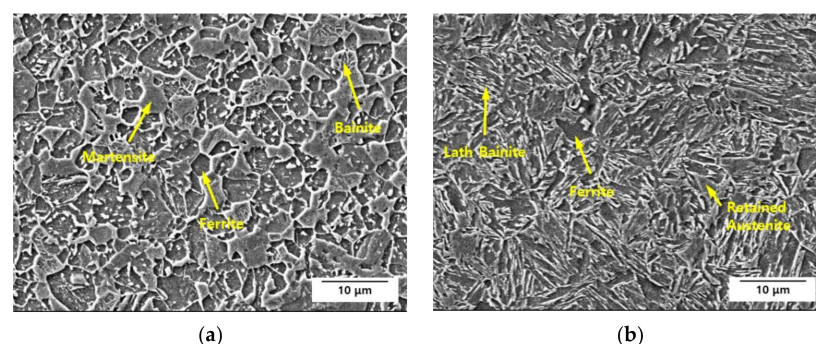


Figure 1. Scanning electron microscopy images of the microstructure of (a) Steel A and (b) Steel B etched with a 2% nital solution.

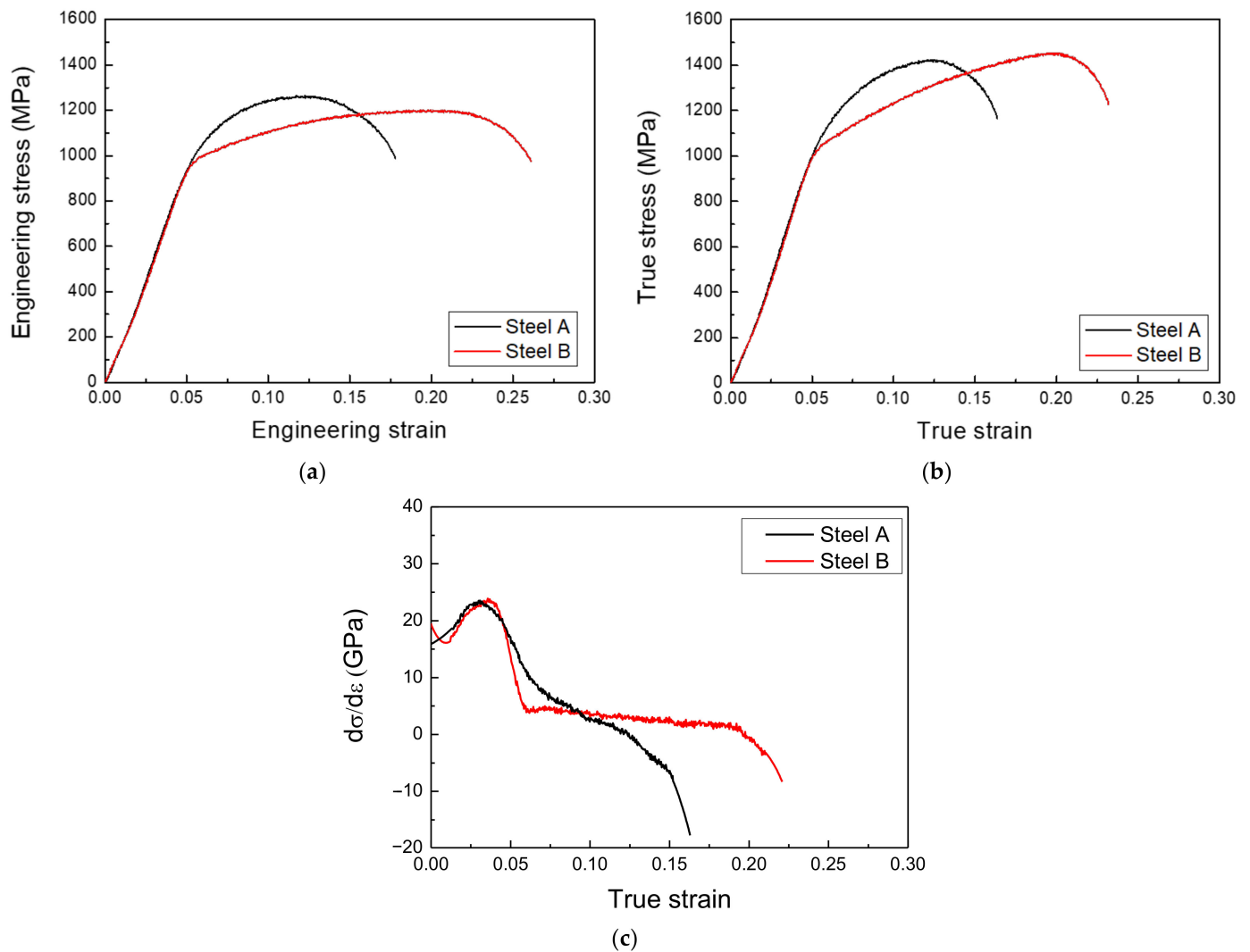


Figure 2. (a) Engineering stress–strain curves, (b) true stress–strain curves, and (c) strain-hardening rate vs. true strain curves for Steel A and Steel B obtained by tensile tests.

2.1. Electrochemical Tests

Potentiodynamic polarization test was performed to analyze the corrosion behavior of AHSSs and determine the applied potentials in the SSRTs. For the electrochemical tests, the specimens were cut into dimensions of $1.5 \times 1.5 \text{ cm}^2$, abraded up to #600 with silicon-carbide paper, degreased with ethanol, and dried with N_2 gas. The electrochemical test environment used a modified Society of Automotive Engineers' (M-SAE) solution at 25°C (room temperature) (see Table 2 for the chemical compositions). All the electrochemical experiments were performed with a triple-electrode electrochemical cell, as shown in Figure 3. The counter electrode was a graphite rod, and the reference electrode was a saturated calomel electrode (SCE). The open-circuit potential (OCP) was established over 3 h. Potentiodynamic polarization tests were conducted with a potential sweep of 0.166 mV/s in accordance with ASTM G5. After the samples were stabilized in an M-SAE solution at room temperature for 1 h, SSRTs were conducted under applied potentials (E_{app}) of -600 , -750 , and $-1500 \text{ mV}_{\text{SCE}}$ based on the potentiodynamic polarization test.

Table 2. Chemical composition (wt.%) of the modified Society of Automotive Engineers' solution.

NaCl	CaCl ₂	NaHCO ₃	(NH ₄) ₂ SO ₄	pH
0.5	0.1	0.075	0.35	7.3

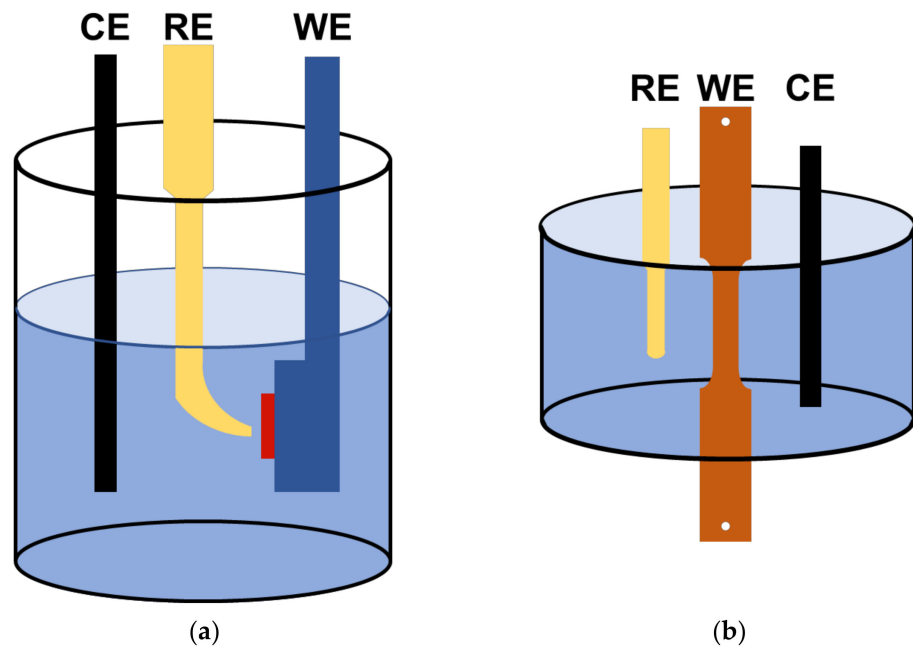


Figure 3. Schematic diagram of the three-electrode cell configuration used in (a) potentiodynamic polarization test and (b) SSRTs. CE, RE, and WE refer to counter electrode, reference electrode, and working electrode, respectively.

2.2. Slow Strain Rate Tests

A schematic image of the specimen for the SSRTs is presented in Figure 4. First, the critical strain rate was determined by various SSRTs in the OCP state; then, under the E_{app} values listed in Section 2.1, SSRTs were conducted at a strain rate of 10^{-5} . After the tests, each fractured specimen was cleaned with ethanol and transferred into liquid nitrogen as soon as possible. Then, the fracture surface was observed via scanning electron microscopy (SEM), and the hydrogen desorption rate was determined by a TDS analysis of the hydrogen content charged into the specimen. To enable the TDS analysis of the hydrogen content, the specimen was cut up to 10 mm from the fracture surface. To calculate the activation energy for hydrogen de-trapping, heating rates of $2\text{ }^{\circ}\text{C}/\text{min}$ and $4\text{ }^{\circ}\text{C}/\text{min}$ were used.

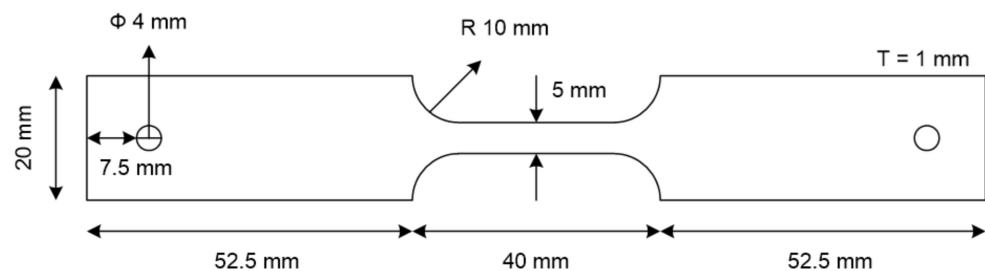


Figure 4. Dimensions of the specimen used in slow strain rate tests.

2.3. Analyses for Hydrogen-Trapping Sites

The grain boundary areas and austenite phase fractions of the samples were measured using electron backscattered diffraction (EBSD). X-ray diffraction (XRD) was performed at a scan rate of $1^{\circ}/\text{min}$, and the dislocation density was calculated using the full width at half-maximum (FWHM). Electron probe microanalysis (EPMA) and transmission electron microscopy (TEM) were used to analyze the type and characteristics of the precipitates. Before EPMA, each specimen was etched slightly with a 2% nital solution for 5 s.

3. Results and Discussion

3.1. Potentiodynamic Polarization Test

This study conducted potentiodynamic polarization tests to analyze the electrochemical properties of the specimens; the results are presented in Figure 5 and Table 3. Mild steel with a tensile strength of 270 MPa was used as a comparison material for the AHSS. The AHSSs exhibited higher corrosion rates than the mild steel. The anodic polarization curves of the AHSSs and the mild steel material were similar in shape; however, the cathodic polarization curve of the AHSSs shifted more to the right compared with the mild steel. This was because hydrogen evolution reactions are more likely in AHSS than in mild steel due to the higher levels of precipitates, carbides, and grain boundary densities. Additionally, there are more phase types in AHSS compared with mild steel, resulting in higher corrosion rates due to the large micro-galvanic effect between phases [17].

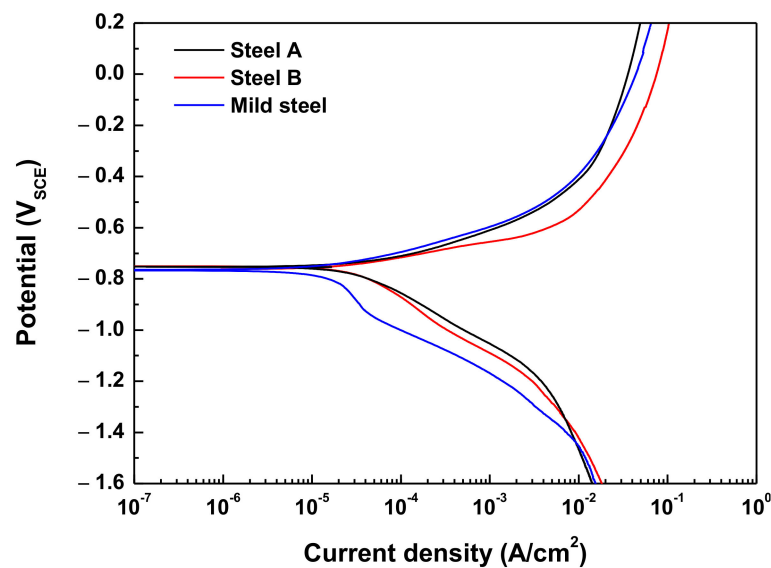
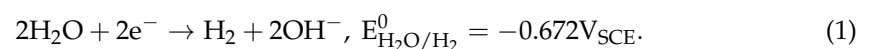


Figure 5. Potentiodynamic polarization curves in a modified Society of Automotive Engineers' solution.

Table 3. Potentiodynamic polarization test results.

Specimen	E_{corr} (V_{SCE})	I_{corr} (A/cm^2)	β_a (mV/Decade)	β_c (mV/Decade)	Corrosion Rate (mm/y)
Steel A	-0.748	3.54×10^{-5}	92	205	0.41
Steel B	-0.755	3.38×10^{-5}	61	241	0.39
Mild steel	-0.765	1.70×10^{-5}	89	419	0.20

The electrochemical properties of both AHSSs, e.g., corrosion potential and corrosion current density, were almost identical. From the polarization curve of Steel A, the redox reaction of hydrogen (Equation (1)) produced a higher hydrogen equilibrium potential ($E_{\text{H}_2\text{O}/\text{H}_2}^0, -0.672 V_{\text{SCE}}$) than corrosion potential ($E_{\text{corr}}, -0.728 V_{\text{SCE}}$). Therefore, hydrogen was also generated at the corrosion potential.



3.2. Slow Strain Rate Tests

During an SSRT, the applied strain rate will cause differences in the occurrence of SCC and HE behaviors [18]. When the strain rate is too high, there is insufficient time for SCC to occur, resulting in only a tensile rupture. Conversely, at a low strain rate, the re-passivation

of the film before the propagation of a crack by anodic dissolution means that SCC does not occur. However, HE does not require the breakdown of the passive film; instead, it is caused by hydrogen trapping inside the steel. Therefore, the lower strain rate requires more time for the hydrogen to be entrapped in the steel, making it more susceptible to HE. Accordingly, when conducting SSRTs to determine the HE characteristics, an optimal strain rate should be applied in consideration of the hydrogen trapping time. To determine the critical strain rate, the SSRTs were performed at strain rates of $2 \times 10^{-4}/s$, $10^{-4}/s$, $10^{-5}/s$, $10^{-6}/s$, and $5 \times 10^{-7}/s$ in M-SAE solution under an OCP state (see Figure 6 for the results). When the strain rate was $10^{-5}/s$, the SSRT results revealed a relatively low elongation for both AHSSs. Therefore, the final SSRTs were performed under a strain rate of $10^{-5}/s$.

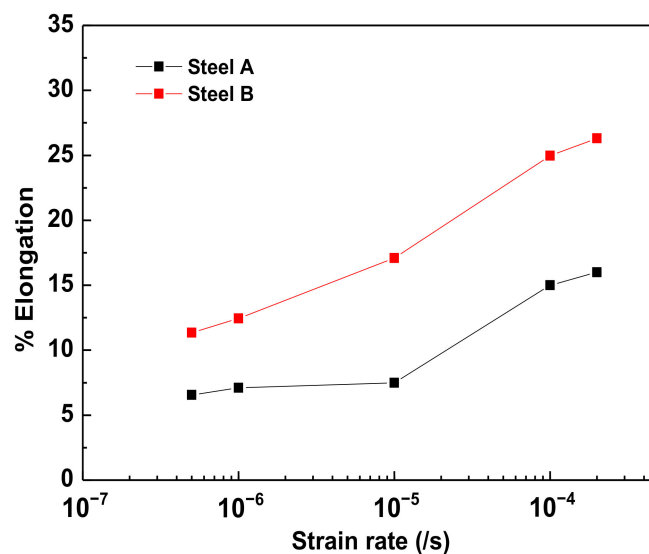


Figure 6. Elongation vs. strain rate in a modified Society of Automotive Engineers' solution under an open-circuit potential state.

Both specimens showed a decreasing elongation with a decreasing strain rate, which is representative of a typical HE elongation–strain rate curve, in which a ductility minimum is not expected [18]. A low strain rate provides sufficient time for lattice diffusion, which allows hydrogen to easily enter the trapping sites.

To minimize the hydrogen generation reactions, the applied anodic potential should be higher than the hydrogen reduction potential. Accordingly, as is shown in Figure 7 and Table 4, the SSRTs in this study were conducted using various E_{app} values. The amounts of hydrogen evolution for the E_{app} values of -1500 mV_{SCE} were calculated by integrating the base area of the current–time curves (Figure 7c,d). Since the current obtained with an E_{app} above -750 mV_{SCE} was caused by corrosion, the hydrogen evolution amounts for E_{app} values of -750 mV_{SCE} were calculated using Faraday's law as follows [18]:

$$m = \frac{I_{red, H_2O/H_2} \times t \times a}{n \times F} \quad (2)$$

where m is the reaction mass (hydrogen evolution amount, in grams), I_{red} is the current of the reduction reaction at each E_{app} (A), t is the time to fracture (s), a is the atomic weight (g/mol), n is the number of electrons ($n = 2$ for Equation (1)), and F is the Faraday constant (96,500 C/mol).

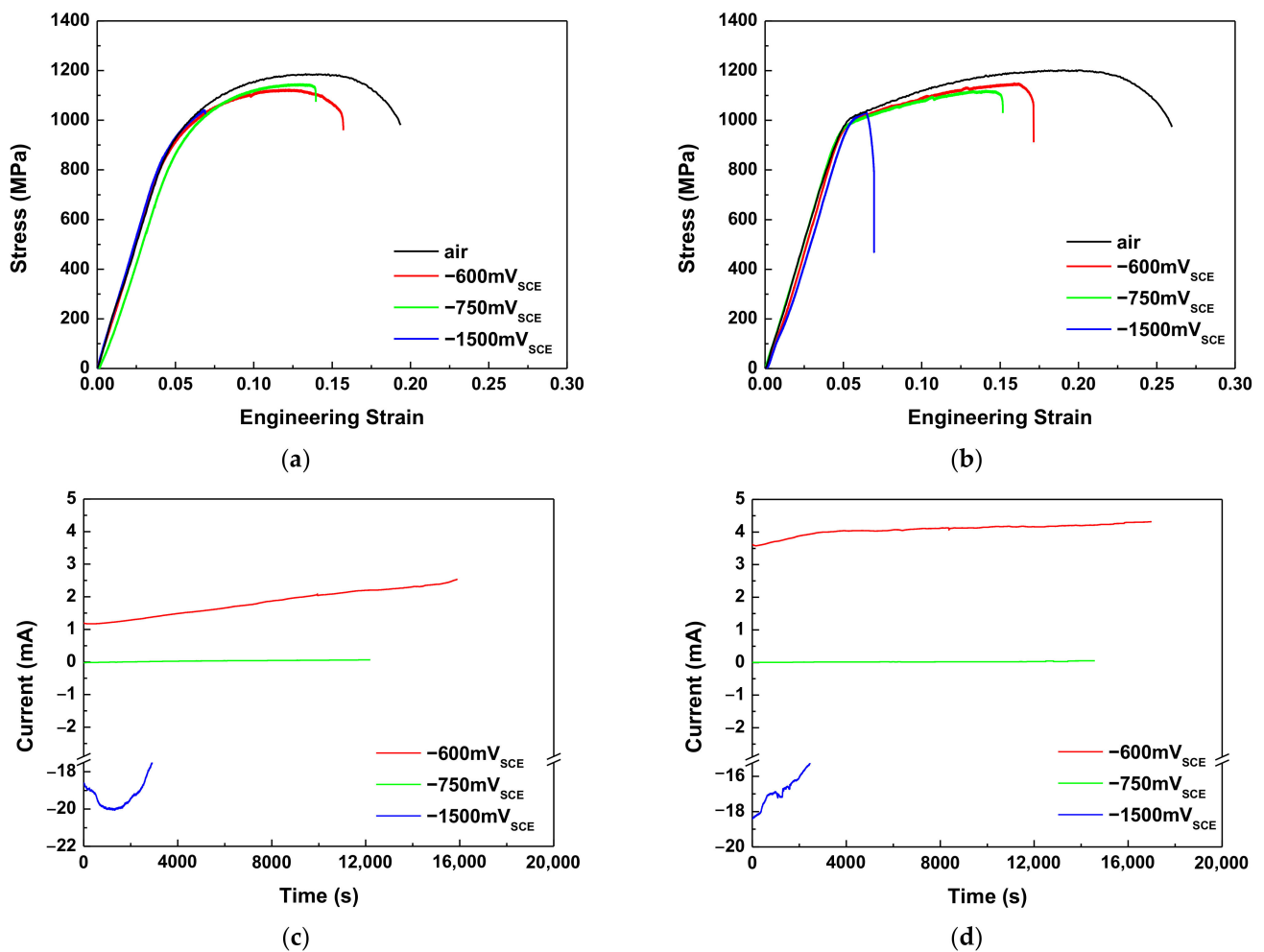


Figure 7. Stress–strain curves for (a) Steel A and (b) Steel B, and the current–time curves of (c) Steel A and (d) Steel B obtained during slow strain rate tests.

Table 4. Slow strain rate test results.

Steel	Applied Potential (mV _{SCE})	Yield Strength (MPa)	Tensile Strength (MPa)	Elongation (%)	HE Susceptibility Index, I _{HE} (%)	Hydrogen Evolution Rate (g)
Steel A	Air	781	1186	16.0	-	-
	-600	703	1124	14.1	11.9	-
	-750 (E _{corr})	699	1146	11.2	30.1	5.76 × 10 ⁻⁶
	-1500	690	1041	4.6	71.0	1.23 × 10 ⁻³
Steel B	Air	800	1202	21.6	-	-
	-600	906	1150	16.4	24.0	-
	-750 (E _{corr})	852	1119	13.3	38.3	2.62 × 10 ⁻⁶
	-1500	851	1034	3.7	82.9	9.76 × 10 ⁻⁴

For both AHSSs, the lower E_{app} was found to be correlated with a reduced elongation. There was an increase in the amount of corrosion with a higher anodic overvoltage, while the hydrogen evolution amount increased with the increasing cathodic overvoltage. A slightly higher amount of hydrogen was generated on Steel A compared to on Steel B.

The HE sensitivity index (I_{HE}) indicates the ductility loss of the AHSSs according to the E_{app} . Since the ductility loss of AHSSs with cathodic applied potential is related to HE, the I_{HE} was used to compare the HE resistance. The I_{HE} can be calculated using Equation (3), in which a higher I_{HE} is associated with increased HE sensitivities. The I_{HE} of

Steel B was approximately 10% higher than that of Steel A. Therefore, compared with Steel B, Steel A had a superior HE resistance.

$$I_{HE} = \frac{\epsilon_{air} - \epsilon_{soln.}}{\epsilon_{air}} \times 100 \quad (3)$$

where I_{HE} is the HE sensitivity index (%), ϵ_{air} is the elongation tested in air, and $\epsilon_{soln.}$ is the elongation tested under an E_{app} .

3.3. Fractography

To determine the fracture properties of the AHSS samples, after the SSRTs were conducted, the fracture surfaces and sides of the specimens were observed by SEM. The results are presented in Figures 8 and 9. Cracks were initiated and propagated from the sides in all the specimens. In Steel A, uniform pitting corrosion was observed on the sides at -600 mV_{SCE}, while there was no changes at -750 and -1500 mV_{SCE} (Figure 8b,f,j). Dimples were observed at the crack initiation site at -600 mV_{SCE}, cleavage occurred at the crack initiation site at -750 mV_{SCE}, and transgranular fracturing was noted at -1500 mV_{SCE} (Figure 8c,g,k). All the specimens exhibited dimpling at the center of their fracture surfaces (Figure 8d,h,l). Steel A only exhibited ductile fracturing at -600 mV_{SCE}, and the lower E_{app} values resulted in more brittle fracture behavior. Even under a potential of -1500 mV_{SCE}, the center of the specimen exhibited ductile fracture behavior. Therefore, hydrogen did not diffuse into the center of the specimen.

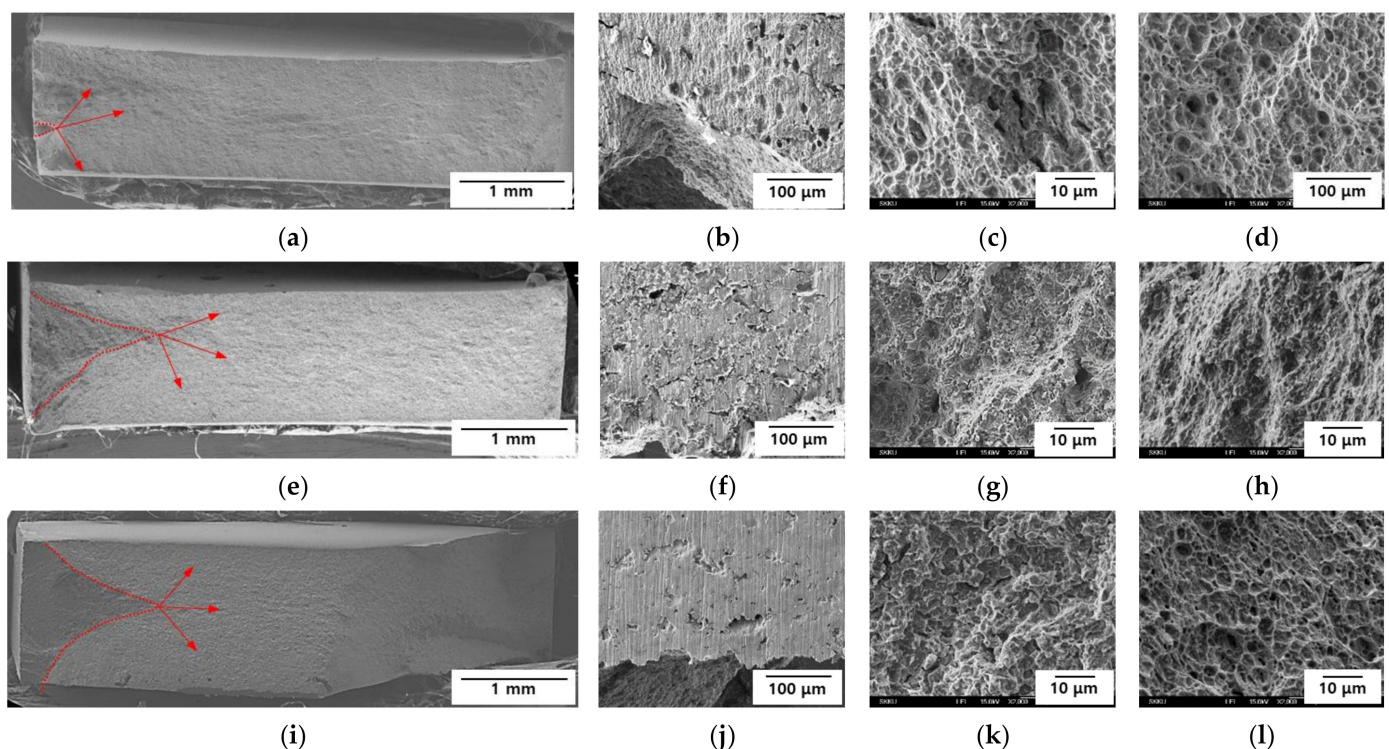


Figure 8. Fractography of Steel A at (a–d) -600 mV_{SCE}, (e–h) -750 mV_{SCE}, and (i–l) -1500 mV_{SCE}. (a,e,i) Entire sample, (b,f,j) side view, (c,g,k) crack initiation site, and (d,h,l) center. Red arrows indicate the initiation of cracks and direction of propagation.

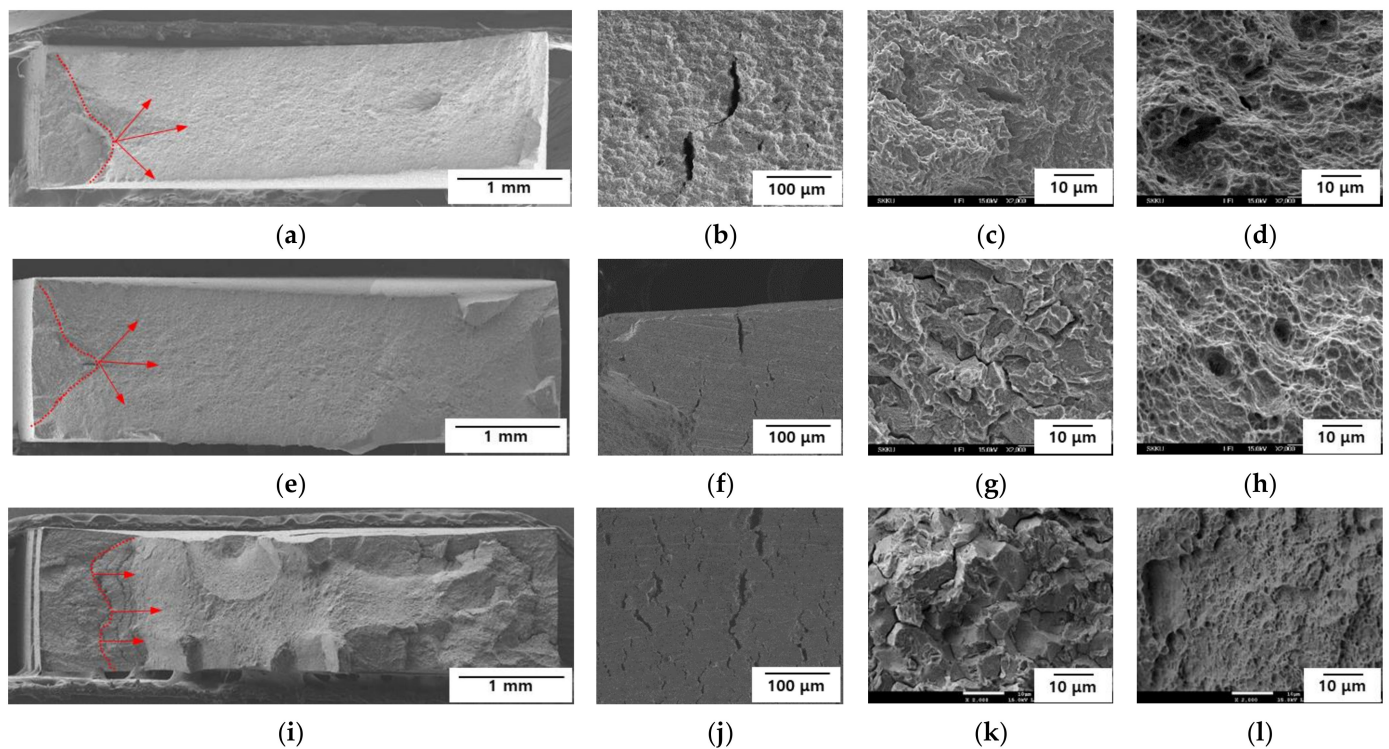


Figure 9. Fractography of Steel B at (a–d) $-600\text{ mV}_{\text{SCE}}$, (e–h) $-750\text{ mV}_{\text{SCE}}$, and (i–l) $-1500\text{ mV}_{\text{SCE}}$. (a,e,i) Entire sample, (b,f,j) side view, (c,g,k) crack initiation site, and (d,h,l) center. Red arrows indicate the initiation of cracks and direction of propagation.

In Steel B, uniform corrosion and cracks occurred on the side of the specimen at $-600\text{ mV}_{\text{SCE}}$. Cracks without any corrosion were observed at -750 and $-1500\text{ mV}_{\text{SCE}}$ (Figure 9b,f,j), and the lower E_{app} values were correlated with a higher density of cracks. Cleavage was observed at the crack initiation site at $-600\text{ mV}_{\text{SCE}}$, while mixed intergranular and transgranular fractures were seen at the crack initiation sites of -750 and $-1500\text{ mV}_{\text{SCE}}$ (Figure 9c,g,k). The intergranular fracture was more obvious at $-1500\text{ mV}_{\text{SCE}}$, and in all the specimens, dimples occurred at the center of the fracture surfaces (Figure 9d,h,l). Steel B exhibited brittle fractures at $-600\text{ mV}_{\text{SCE}}$, and the lower E_{app} values were associated with more obvious brittle fracture behaviors. At $-1500\text{ mV}_{\text{SCE}}$, the center of Steel B demonstrated ductile fracture behavior. Thus, like Steel A, hydrogen did not diffuse into the center of the specimen. Under the same E_{app} , Steel B exhibited more brittle fracture behavior than Steel A. The fractography results confirmed that, compared with Steel A, Steel B was more susceptible to delayed fractures.

3.4. Hydrogen Trapping and Desorption Behaviors

To investigate the desorption behavior of diffusible hydrogen, the SSRT specimens were analyzed by TDS at the E_{app} values of -600 , -750 , and $-1500\text{ mV}_{\text{SCE}}$. The results are presented in Figure 10 and Table 5. To quantitatively analyze the desorbed hydrogen, the area below the desorption rate vs. the temperature curve was integrated [19] (see Table 5 for the results). Just 0.05 ppm of diffusible hydrogen was released in the as-received specimens. Most of the diffusible hydrogen that accumulated during the steel manufacturing process (e.g., during acid cleaning) appeared to be released during machining and storage. However, when the potential was applied, the lower E_{app} was associated with the higher hydrogen desorption rate. Under the same E_{app} values of both AHSSs, the desorbed diffusible hydrogen content of Steel B was higher than in Steel A, except for $-1500\text{ mV}_{\text{SCE}}$. In that case, Peak 3 of Steel A and Peak 2 of Steel B (located at approximately $220\text{ }^{\circ}\text{C}$) originated from the deformation field around the dislocation. In this study, as tensile deformation was considered an error, the hydrogen de-trapping from these peaks was negligible.

Theoretically, the production of hydrogen did not occur at $-600\text{ mV}_{\text{SCE}}$, although diffusible hydrogen was detected. It is assumed that the hydrogen was accumulated from the 1-h stabilizing process before the SSRTs were conducted.

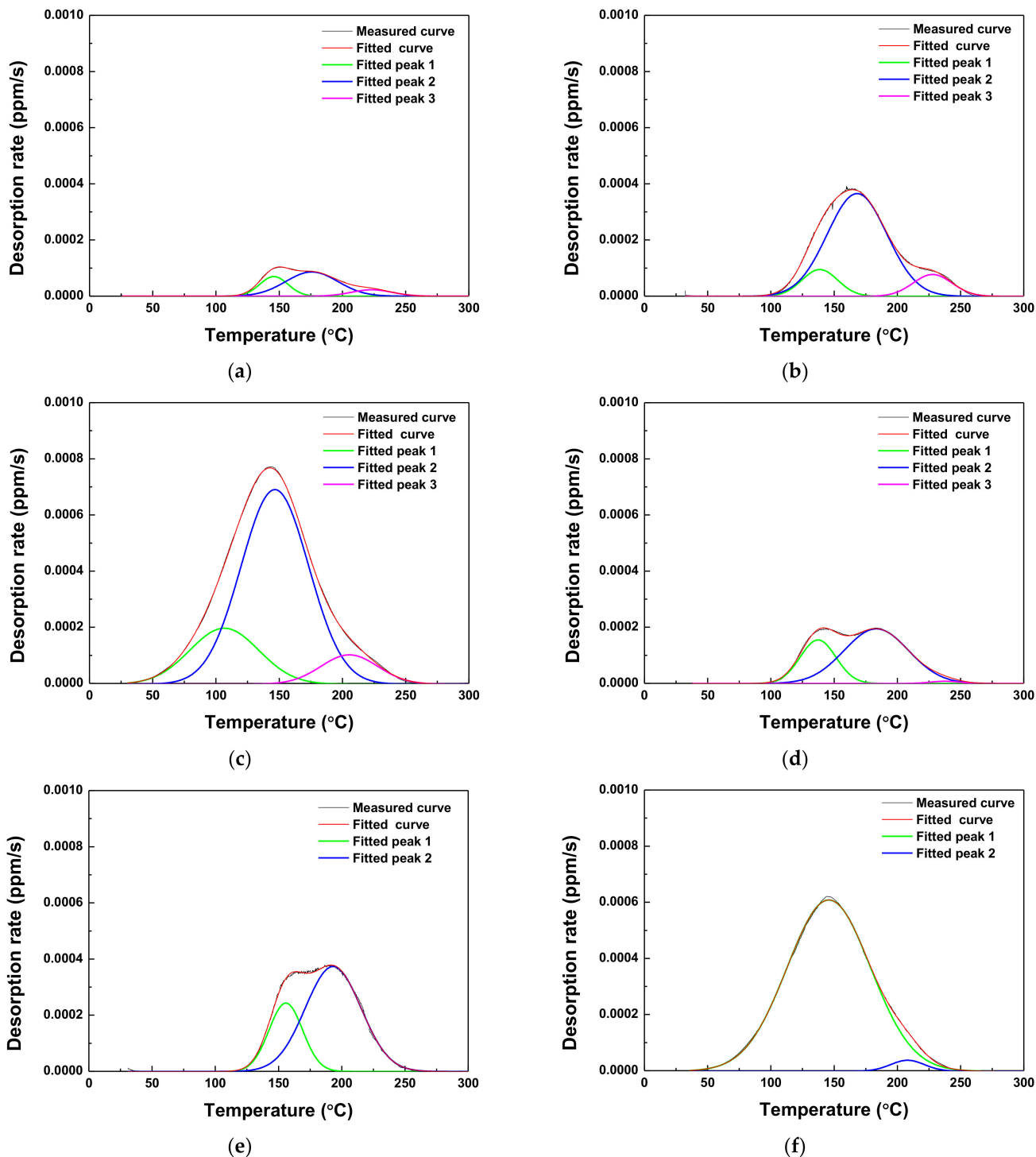


Figure 10. Cont.

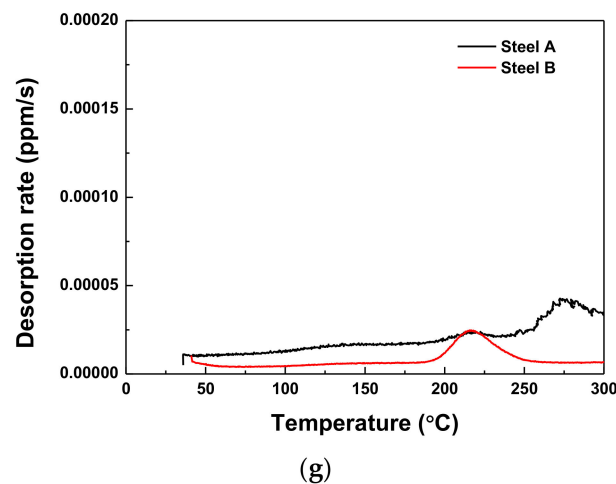


Figure 10. Hydrogen desorption rates obtained by thermal desorption spectroscopy at a heating rate of 4 °C/min in a fractured specimens of (a–c) Steel A and (d–f) Steel B at (a,d) –600, (b,e) –750, (c,f) –1500 mV_{SCE}, and (g) the as-received condition.

Table 5. Desorbed hydrogen contents for each peak.

Steel	Applied Potential (mV _{SCE})	Peak 1 (ppm)	Peak 2 (ppm)	Peak 3 (ppm)	Sum of Peaks (ppm)
Steel A	As-received	0.0569	-	-	0.0569 ± 0.0323
	–600	0.0622	0.1511	0.0311	0.2485 ± 0.1262
	–750	0.0579	0.3693	0.0514	0.4787 ± 0.0145
	–1500	0.2264	0.7735	0.0978	1.0977 ± 0.0968
Steel B	As-received	0.0506	-	-	0.0506 ± 0.0268
	–600	0.1388	0.3122	0.0057	0.4568 ± 0.2070
	–750	0.1748	0.4445	-	0.6193 ± 0.1280
	–1500	0.9622	0.0246	-	0.9868 ± 0.0052

To analyze the hydrogen-trapping sites in the steel specimens, the activation energy for hydrogen de-trapping was calculated using Equation (4), as proposed by Kissinger [20–22]:

$$\frac{\partial \ln(\varphi/T_c^2)}{\partial(1/T_c)} = -\frac{E_{aT}}{R} \quad (4)$$

where T_c is the temperature (K) at which the hydrogen desorption rate is maximal, φ is the heating rate (K/min), E_{aT} is the activation energy for hydrogen de-trapping (kJ/mol), and R is the ideal gas constant (8.314 J/K·mol).

As is shown in Figure 10, the desorption curves were deconvoluted into two or three peaks of Gaussian curves, indicating that diffusible hydrogen accumulated at more than two or three trapping sites. According to the Kissinger equation, the slope of $\ln(\varphi/T_c^2)$ vs. $1/T_c$ curve for each peak represents the activation energies (see Figure 11 for the results). The activation energies for Steels A and B corresponding to each peak are illustrated in Table 6.

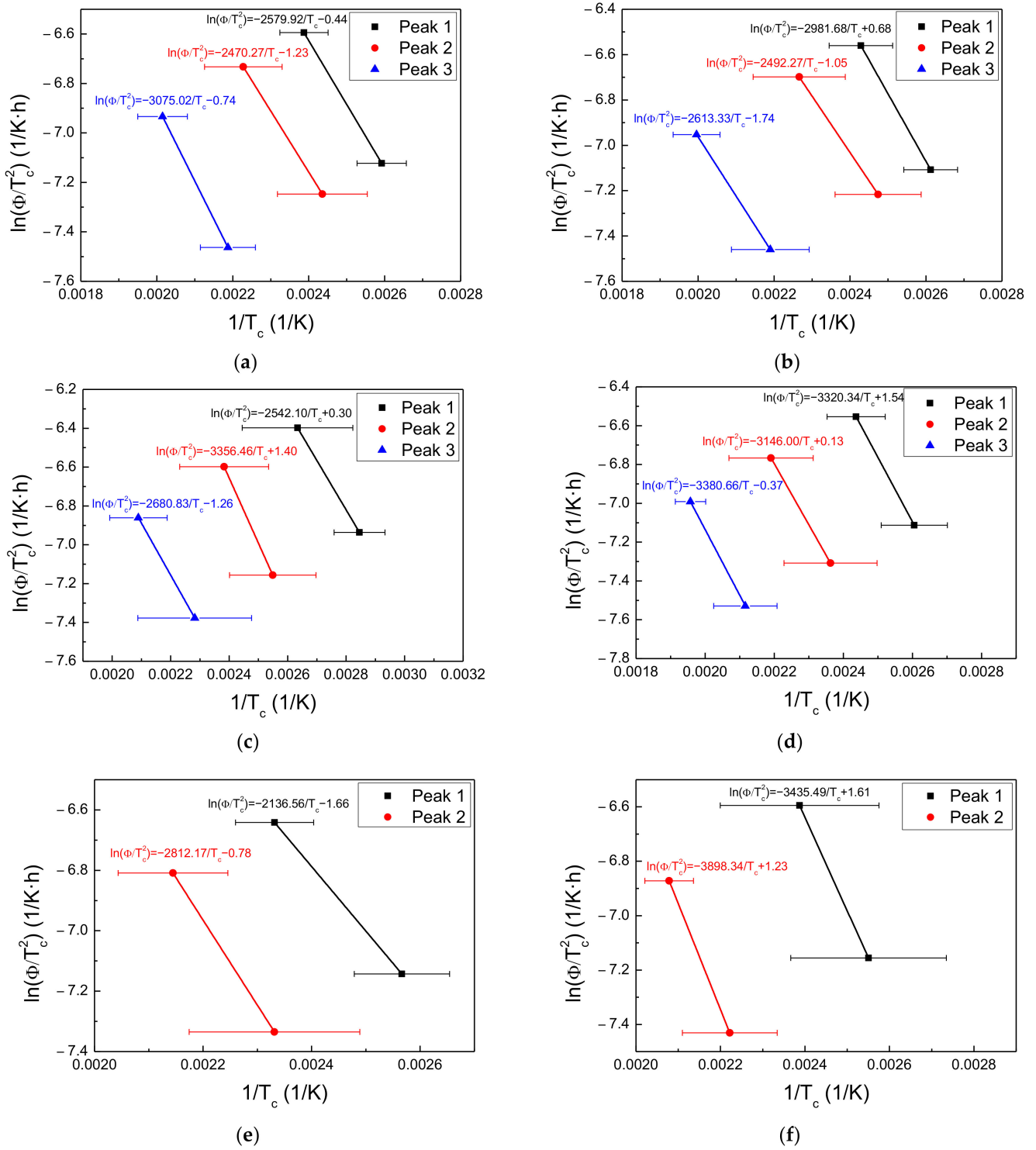


Figure 11. $\ln(\phi/T_c^2)$ vs. $1/T_c$ curve for (a–c) Steel A and (d–f) Steel B at (a,d) –600, (b,e) –750, and (c,f) –1500 mV_{SCE}.

Table 6. Calculated activation energies for hydrogen de-trapping.

Steel	Applied Potential (mV _{SCE})	Peak 1 (kJ/mol)	Peak 2 (kJ/mol)	Peak 3 (kJ/mol)
Steel A	−600	21.5	20.5	25.6
	−750	24.8	20.7	21.7
	−1500	21.1	27.9	22.3
Steel B	−600	27.6	26.1	28.1
	−750	17.8	23.4	-
	−1500	28.6	32.4	-

Table 7 summarizes the activation energies for hydrogen de-trapping reported in previous related studies. Based on the published literature, the electrochemically accumulated hydrogen corresponding to Peaks 1 and 2 in Steel A was associated with the grain boundary and dislocation. Peak 3 was associated with the mechanical deformation by tensile deformation that occurred during the SSRTs [23]. For Steel B, the hydrogen corresponding to Peaks 1 and 2 at −600 and −750 mV_{SCE}, respectively, was desorbed from the grain boundary, dislocation, and ferrite–Fe₃C interface. In that specimen, the contributions from the grain boundary and dislocation were indistinguishable in Peak 1 at −1500 mV, which means that Peak 1 was the sum of the hydrogen desorbed from the grain boundary and dislocation. Peak 3 (−1500 mV_{SCE}) was associated with mechanical deformation by tensile deformation, which occurred during the SSRTs.

Table 7. Types of reversible and irreversible hydrogen-trapping sites reported in the literature.

Type of Trap	Activation Energy (kJ/mol)	References
Reversible hydrogen-trapping sites		
Ferrite/Fe ₃ C	10.9	[16]
Grain boundary	17.2	[16]
Ferrite/Fe ₃ C interface	18.4	[16,24]
Grain boundary, Dislocation	21–29	[25–28]
Deformation field around dislocation	29 ± 5	[23]
Irreversible hydrogen-trapping sites		
Semi-coherent TiC	49.9	[28]
High-angle grain boundary	53–59	[29]
NbC interface	63–68	[30]
Incoherent TiC	85.7, 86.9	[28]

3.5. Analysis of Defects Acting as Hydrogen Trapping Sites

3.5.1. Electron Backscattered Diffraction Analysis

EBSD analysis was conducted to measure the grain boundary density and fraction of retained austenite; the results are shown in Figure 12 and Table 8. Each value was measured three times to derive the mean value. The average grain sizes measured by EBSD for Steel A and Steel B were 2.79 and 4.03 μm, respectively. Mild steel has an average approximate grain size of 22 μm [31]; therefore, these values indicate that AHSSs have a smaller grain size than mild steel.

Table 8. EBSD analysis results (relative value).

Specimen	Average Grain Size	High-Angle Grain Boundary Length	Low-Angle Grain Boundary Length	Retained Austenite Fraction
Steel A	2.79 μm	15.73 mm	1.91 mm	9.5%
Steel B	4.03 μm	13.93 mm	1.99 mm	10.9%

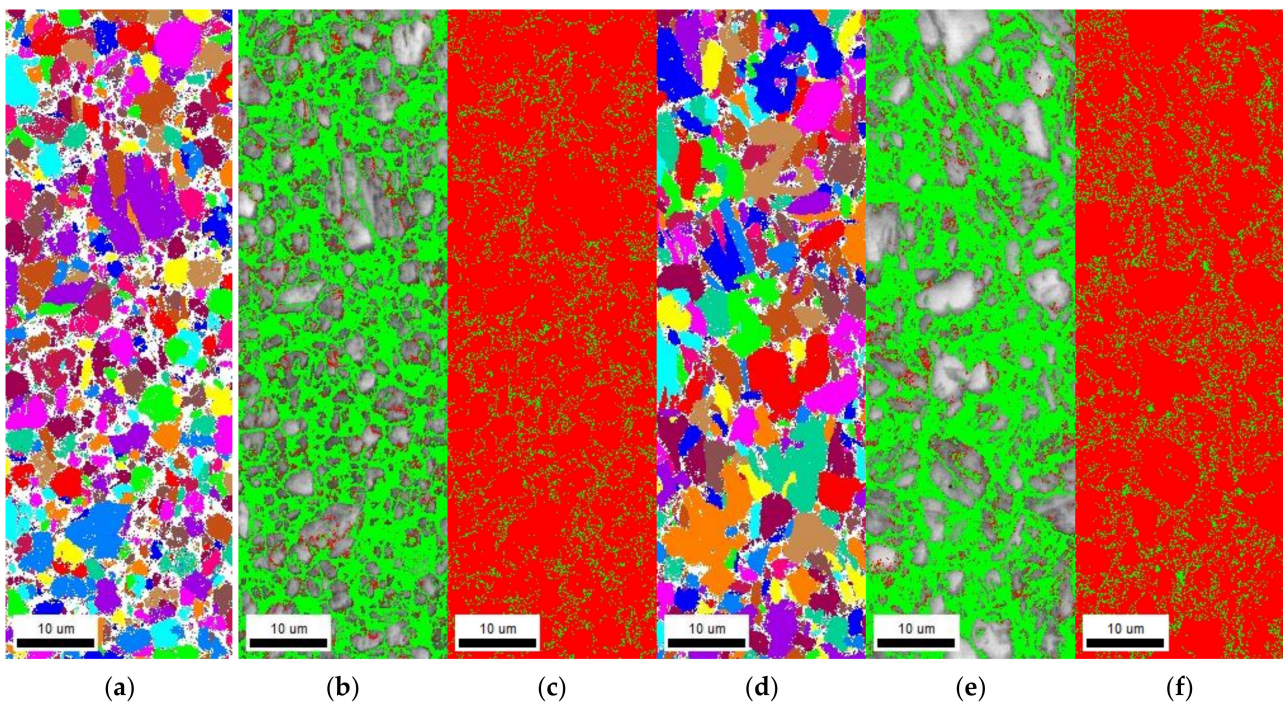


Figure 12. Electron backscattered diffraction results of (a–c) Steel A and (d–f) Steel B. (a,d) Grain mapping. (b,e) Low-angle grain boundary (red) and high-angle grain boundary (green) mapping. (c,f) Face-centered cubic (red) and body-centered cubic (green) mapping.

When the misorientation of a grain boundary exceeds 15° , it is termed a high-angle grain boundary; otherwise, it is a low-angle grain boundary. In this study, Steel A had the longer high-angle grain length than Steel B, and the low-angle grain boundary lengths in both specimens were similar. The low-angle grain boundary is a reversible hydrogen-trapping site, suggesting that a longer low-angle grain boundary is more likely to induce HE [32]. Since the high-angle grain boundary is an irreversible hydrogen-trapping site, the longer high-angle grain boundary enhances the HE resistance. Therefore, in both AHSSs, the diffusible hydrogen content charged in the grain boundary is almost identical, and the non-diffusible hydrogen content charged in the grain boundary of Steel A is expected to be high.

The conducted EBSD analysis reveals that the face-centered cubic (FCC) structure reflected the retained austenite content. In Steel B, the retained austenite fraction was 10.9%, which was 1.4% higher than in Steel A. Retained austenite is an irreversible hydrogen-trapping site that enhances the HE resistance. However, in Steel B, the retained austenite fraction is not proportional to the HE resistance; this is because retained austenite with an FCC structure is transformed by tensile stress into martensite with a body-centered tetragonal (BCT) structure. Since BCT structures have a lower hydrogen solubility and faster diffusion rate than FCC structures, hydrogen accumulation via diffusion is easy in the BCT structure [33]. Thus, the hydrogen charged on the retained austenite in Steel B segregates during the tensile process and becomes susceptible to HE. Furthermore, the austenite–matrix interface is an effective diffusible hydrogen-trapping site [34]. The higher fraction of retained austenite increases the susceptibility to HE, i.e., it is expected that Steel B will be more susceptible to HE than Steel A.

3.5.2. X-ray Diffraction

The dislocation density of the samples was determined using XRD (see Figure 13 for the results). Both AHSSs were mainly comprised of α -Fe, although γ -Fe peaks were also observed. Specifically, the γ -Fe peaks were higher in intensity in Steel B compared with Steel A, which is consistent with the results of the EBSD analysis. The dislocation density is

defined as the length of dislocation lines per unit volume of crystal and can be calculated using the Williamson–Smallman relationship [35], as in Equation (5) below:

$$\delta = \frac{1}{D^2} \quad (5)$$

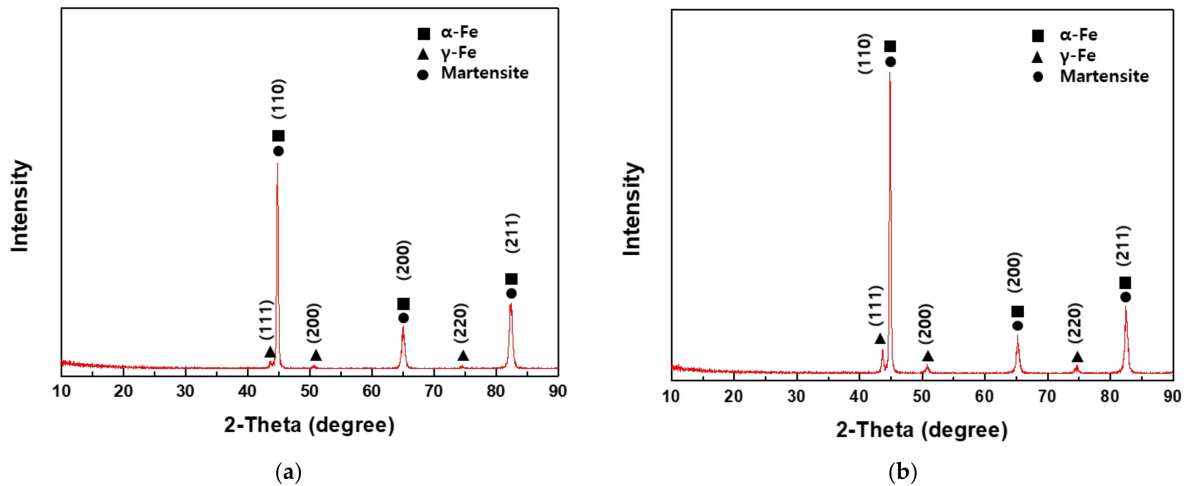


Figure 13. X-ray diffraction results for (a) Steel A and (b) Steel B.

Here, δ is the dislocation density, and D is the size of crystalline domain, which is similar to the grain size. Therefore, D can be calculated using Scherrer's equation [36], as follows:

$$D = \frac{k\lambda}{\beta \cos \theta} \quad (6)$$

in which k is the shape factor (=approx. 0.9), λ is the wavelength (Cu-K α = 1.5406 Å), β is the full width at half-maximum (FWHM) value, and θ is the position of the peaks. Using the above expression, the dislocation density was calculated to be $3.488 \times 10^{14}/\text{m}^2$ and $6.263 \times 10^{14}/\text{m}^2$ for Steel A and Steel B, respectively, i.e., the dislocation density of Steel B was twice that of Steel A. Since the low-angle grain boundary areas of the two AHSSs were similar, the difference in the hydrogen content of the two types of AHSSs discharged during TDS was attributed to the difference in the dislocation density.

3.5.3. Characterization of Precipitates

To characterize the type and size of the precipitates, EPMA and TEM analyses were conducted. The results are presented in Figure 14. According to Figure 14a, the precipitate of Steel A was rich in Ti and Nb and a (Nb, Ti) precipitate surrounded the Ti-rich precipitate. However, in the precipitates of Steel B, only Ti was detected, while Nb was undetected. The precipitates of both AHSSs were approximately 1 μm in size. The TEM images and diffraction patterns for the two types of AHSSs are presented in Figure 14c,d. In Steel A, extremely fine precipitates were distributed along the grain boundary. The electron diffraction pattern and energy-dispersive X-ray spectroscopy analysis confirmed that the precipitates were amorphous Ti and Fe carbides smaller than 10 nm in size. Only the small fraction of Fe carbides was distributed randomly in the grain, and in Steel B, no TiC precipitate was observed (Figure 14d). The EPMA and TEM results revealed the presence of sub-micrometer (Nb, Ti)C and fine TiC precipitates in Steel A, although Steel B contained only a sub-micrometer TiC precipitate. The small size of the carbide produced a large effective area for hydrogen trapping [37,38]. Therefore, Steel A was able to trap considerably more hydrogen in the TiC precipitate interface compared with Steel B. Since Nb and Ti precipitates are powerful and irreversible hydrogen-trapping sites, they can positively influence HE resistance, i.e., Steel A is expected to be more resistant to HE than Steel B.

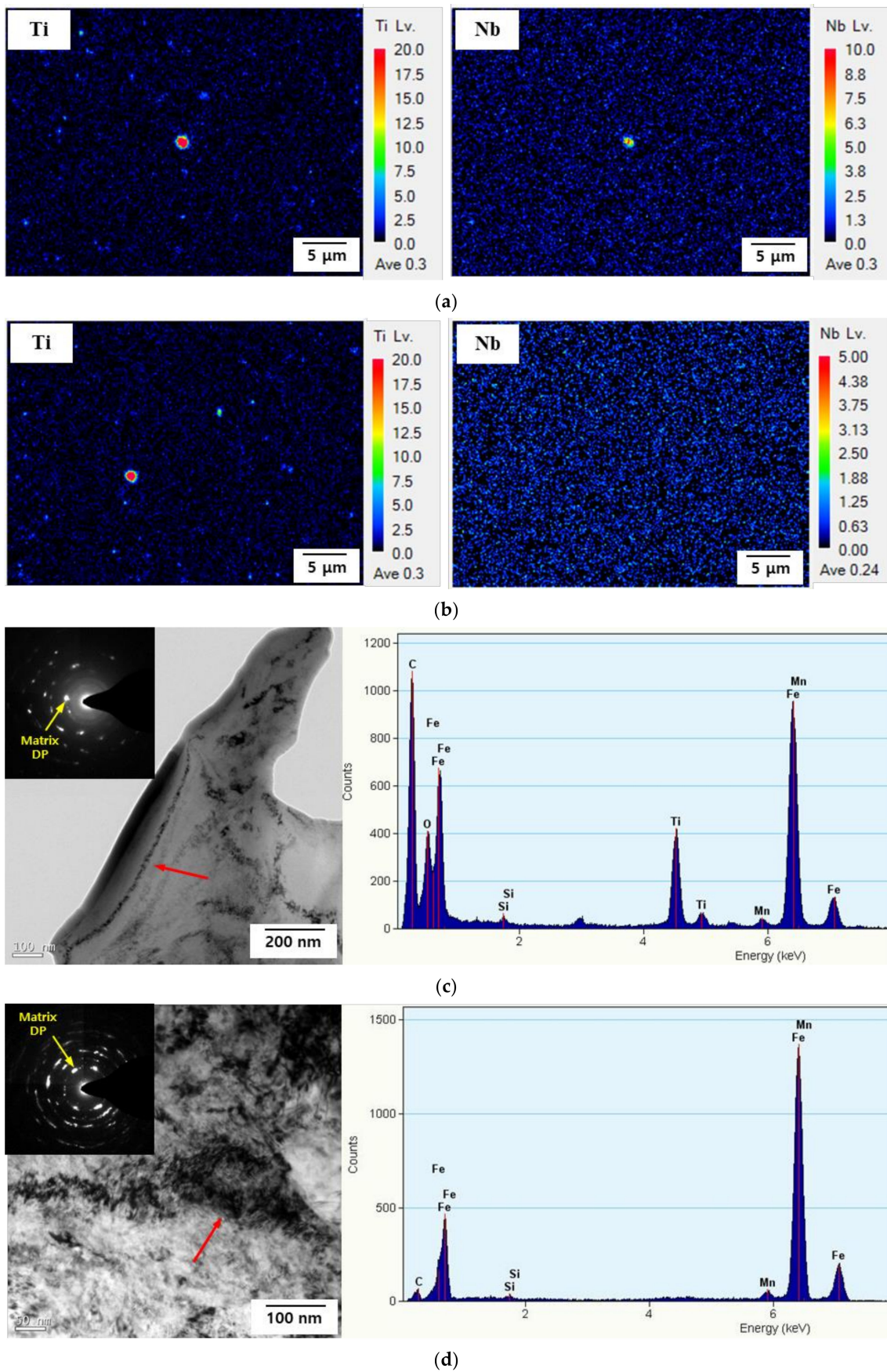


Figure 14. Identification of the types and sizes of precipitates on each AHSSs. Electron probe microanalysis results for (a) Steel A and (b) Steel B. Transmission electron microscopy results for (c) Steel A and (d) Steel B.

4. Conclusions

This study investigated the SCC and HE mechanisms of two AHSSs using SSRTs and characterized their hydrogen-trapping behaviors using TDS, EBSD, and XRD. According to the results of these investigations, the SCC and HE characteristics of the studied AHSSs can be summarized as follows:

1. For both AHSSs, elongation decreased as the cathodic overvoltage increased, i.e., both types of AHSSs were fractured by the mechanism of HE. Even when the anodic potential was applied, HE was more dominant than SCC. Although the HE sensitivity of Steel B was higher than that of Steel A, both AHSSs were more sensitive to HE than SCC.
2. In both AHSSs, the lower E_{app} was associated with a strong brittle fracture behavior. However, the center of each specimen exhibited ductile fracture behavior, because the hydrogen did not diffuse into that region. It was clear that the fracture surface of Steel B was more brittle than that of Steel A.
3. The lower E_{app} was associated with the higher rate of hydrogen desorption. In both AHSSs, diffusible hydrogen was trapped mainly at the grain boundary and dislocation.
4. The density of the irreversible hydrogen-trapping sites (high-angle grain boundaries and TiC precipitates) was higher in Steel A than in Steel B. However, the density of the reversible hydrogen-trapping sites (low-angle grain boundaries and dislocations) was lower in Steel A than in Steel B. Therefore, compared to Steel A, Steel B was more susceptible to HE.

Author Contributions: Conceptualization, S.C. and G.-I.K.; methodology, S.C. and G.-I.K.; validation, S.C., G.-I.K., S.-J.K., J.-S.Y., Y.-S.J., Y.-H.Y. and J.-G.K.; formal analysis, S.C. and G.-I.K.; investigation, S.C. and G.-I.K.; resources, S.C. and G.-I.K.; data curation, S.C., G.-I.K., S.-J.K. and J.-S.Y.; writing—original draft preparation, S.C. and G.-I.K.; writing—review and editing, S.C., G.-I.K., S.-J.K., J.-S.Y., Y.-S.J., Y.-H.Y. and J.-G.K.; visualization, S.C. and G.-I.K.; supervision, J.-G.K.; project administration, J.-G.K.; and funding acquisition, J.-G.K. All authors have read and agreed to the published version of the manuscript.

Funding: This research was funded by the POSCO (Grant Number 2019Z083).

Institutional Review Board Statement: Not applicable.

Informed Consent Statement: Not applicable.

Data Availability Statement: Not applicable.

Acknowledgments: This research was supported by SungKyunKwan University and BK21 FOUR (Graduate School Innovation) funded by the Ministry of Education (MOE, Korea) and the National Research Foundation of Korea (NRF).

Conflicts of Interest: The authors declare no conflict of interest.

References

1. Miller, W.; Zhuang, L.; Bottema, J.; Wittebrood, A.J.; De Smet, P.; Haszler, A.; Vieregge, A. Recent development in aluminium alloys for the automotive industry. *Mater. Sci. Eng. A* **2000**, *280*, 37–49. [[CrossRef](#)]
2. Kulekci, M.K. Magnesium and its alloys applications in automotive industry. *Int. J. Adv. Manuf. Technol.* **2008**, *39*, 851–865. [[CrossRef](#)]
3. Cole, G.; Sherman, A. Light weight materials for automotive applications. *Mater. Charact.* **1995**, *35*, 3–9. [[CrossRef](#)]
4. Friedrich, H.; Schumann, S. Research for a “new age of magnesium” in the automotive industry. *J. Mater. Process. Technol.* **2001**, *117*, 276–281. [[CrossRef](#)]
5. Musfirah, A.; Jaharah, A. Magnesium and aluminum alloys in automotive industry. *J. Appl. Sci. Res* **2012**, *8*, 4865–4875.
6. Gándara, M.J.F. Recent growing demand for magnesium in the automotive industry. *Mater. Technol.* **2011**, *45*, 633–637.
7. Tisza, M.; Czinege, I. Comparative study of the application of steels and aluminium in lightweight production of automotive parts. *Int. J. Lightweight Mater. Manuf.* **2018**, *1*, 229–238. [[CrossRef](#)]
8. Hirsch, J. Recent development in aluminium for automotive applications. *Trans. Nonferrous Met. Soc. China* **2014**, *24*, 1995–2002. [[CrossRef](#)]

9. Baluch, N.; Udin, Z.M.; Abdullah, C.S. Advanced high strength steel in auto industry: An overview. *Eng. Technol. Appl. Sci. Res.* **2014**, *4*, 686–689. [[CrossRef](#)]
10. Galán, J.; Samek, L.; Verleysen, P.; Verbeken, K.; Houbaert, Y. Advanced high strength steels for automotive industry. *Rev. Metal.* **2012**, *48*, 118. [[CrossRef](#)]
11. Funakawa, Y.; Nagataki, Y. High Strength Steel Sheets for Weight Reduction of Automotives. *JFE Tech. Rep.* **2019**, *24*, 1–5.
12. Lovicu, G.; Bottazzi, M.; D'aiuto, F.; De Sanctis, M.; Dimatteo, A.; Santus, C.; Valentini, R. Hydrogen embrittlement of automotive advanced high-strength steels. *Metall. Mater. Trans. A* **2012**, *43*, 4075–4087. [[CrossRef](#)]
13. Khanzhin, V.; Nikulin, S.; Belov, V.; Rogachev, S.; Turilina, V.Y. Hydrogen embrittlement of steels: III. Influence of secondary-phase particles. *Russ. Metall. (Met.)* **2013**, *2013*, 790–796. [[CrossRef](#)]
14. Khanzhin, V.; Turilina, V.Y.; Rogachev, S.; Nikitin, A.; Belov, V. Effect of various factors on hydrogen embrittlement of structural steels. *Met. Sci. Heat Treat.* **2015**, *57*, 197–204. [[CrossRef](#)]
15. Hagi, H.; Hayashi, Y.; Ohtani, N. Diffusion coefficient of hydrogen in pure iron between 230 and 300 K. *Trans. Jpn. Inst. Met.* **1979**, *20*, 349–357. [[CrossRef](#)]
16. Choo, W.; Lee, J.Y. Thermal analysis of trapped hydrogen in pure iron. *Metall. Mater. Trans. A* **1982**, *13*, 135–140. [[CrossRef](#)]
17. Katiyar, P.K.; Misra, S.; Mondal, K. Comparative corrosion behavior of five microstructures (pearlite, bainite, spheroidized, martensite, and tempered martensite) made from a high carbon steel. *Metall. Mater. Trans. A* **2019**, *50*, 1489–1501. [[CrossRef](#)]
18. Jones, D.A. *Principles and Prevention of Corrosion*, 2nd ed.; Prentice Hall: Upper Saddle River, NJ, USA, 1996.
19. Yoo, J.; Xian, G.; Lee, M.; Kim, Y.; Kang, N. Hydrogen embrittlement resistance and diffusible hydrogen desorption behavior of multipass FCA weld metals. *J. Weld. Join.* **2014**, *31*, 112–118. [[CrossRef](#)]
20. Hurley, C.; Martin, F.; Marchetti, L.; Chêne, J.; Blanc, C.; Andrieu, E. Numerical modeling of thermal desorption mass spectroscopy (TDS) for the study of hydrogen diffusion and trapping interactions in metals. *Int. J. Hydrog. Energy* **2015**, *40*, 3402–3414. [[CrossRef](#)]
21. Kirchheim, R. Bulk diffusion-controlled thermal desorption spectroscopy with examples for hydrogen in iron. *Metall. Mater. Trans. A* **2016**, *47*, 672–696. [[CrossRef](#)]
22. Ryu, J.H.; Chun, Y.S.; Lee, C.S.; Bhadeshia, H.; Suh, D.W. Effect of deformation on hydrogen trapping and effusion in TRIP-assisted steel. *Acta Mater.* **2012**, *60*, 4085–4092. [[CrossRef](#)]
23. Krieger, W.; Merzlikin, S.V.; Bashir, A.; Szczepaniak, A.; Springer, H.; Rohwerder, M. Spatially resolved localization and characterization of trapped hydrogen in zero to three dimensional defects inside ferritic steel. *Acta Mater.* **2018**, *144*, 235–244. [[CrossRef](#)]
24. Hong, G.-W.; Lee, J.-Y. The interaction of hydrogen and the cementite-ferrite interface in carbon steel. *J. Mater. Sci.* **1983**, *18*, 271–277. [[CrossRef](#)]
25. Wang, M.; Akiyama, E.; Tsuzaki, K. Effect of hydrogen and stress concentration on the notch tensile strength of AISI 4135 steel. *Mater. Sci. Eng. A* **2005**, *398*, 37–46. [[CrossRef](#)]
26. Hong, G.-W.; Lee, J.-Y. The interaction of hydrogen with dislocation in iron. In *Perspectives in Hydrogen in Metals*; Elsevier: Amsterdam, The Netherlands, 1986; pp. 427–435.
27. Yamasaki, S.; Takahashi, T. Evaluation method of delayed fracture property of high strength steels. *J. Iron Steel Inst. Jpn.* **1997**, *83*, 454–459. [[CrossRef](#)]
28. Wei, F.; Hara, T.; Tsuzaki, K. Precise determination of the activation energy for desorption of hydrogen in two Ti-added steels by a single thermal-desorption spectrum. *Metall. Mater. Trans. B* **2004**, *35*, 587–597. [[CrossRef](#)]
29. Pressouyre, G. A classification of hydrogen traps in steel. *Metall. Mater. Trans. A* **1979**, *10*, 1571–1573. [[CrossRef](#)]
30. Wallaert, E.; Depover, T.; Arafin, M.; Verbeken, K. Thermal desorption spectroscopy evaluation of the hydrogen-trapping capacity of NbC and NbN precipitates. *Metall. Mater. Trans. A* **2014**, *45*, 2412–2420. [[CrossRef](#)]
31. Jangir, D.K.; Verma, A.; Sankar, K.M.; Khanna, A.; Singla, A. Influence of grain size on corrosion resistance and electrochemical behaviour of mild steel. *Int. J. Res. Appl. Sci. Eng. Technol.* **2018**, *6*, 2875–2881. [[CrossRef](#)]
32. Oger, L.; Malard, B.; Odemer, G.; Peguet, L.; Blanc, C. Influence of dislocations on hydrogen diffusion and trapping in an Al-Zn-Mg aluminium alloy. *Mater. Des.* **2019**, *180*, 107901. [[CrossRef](#)]
33. Kang, H.-J.; Kang, N.-H.; Park, S.-J.; Chang, W.-S. Evaluation of hydrogen delayed fracture for high strength steels and weldments. *J. Weld. Join.* **2011**, *29*, 33–39. [[CrossRef](#)]
34. Szost, B.A.; Vegter, R.H.; Rivera-Díaz-del-Castillo, P.E. Hydrogen-trapping mechanisms in nanostructured steels. *Metall. Mater. Trans. A* **2013**, *44*, 4542–4550. [[CrossRef](#)]
35. Shahmoradi, Y.; Souri, D.; Khorshidi, M. Glass-ceramic nanoparticles in the Ag₂O–TeO₂–V₂O₅ system: Antibacterial and bactericidal potential, their structural and extended XRD analysis by using Williamson–Smallman approach. *Ceram. Int.* **2019**, *45*, 6459–6466. [[CrossRef](#)]
36. Bykkam, S.; Ahmadipour, M.; Narisngam, S.; Kalagadda, V.R.; Chidurala, S.C. Extensive studies on X-ray diffraction of green synthesized silver nanoparticles. *Adv. Nanopart* **2015**, *4*, 1–10. [[CrossRef](#)]
37. Yamasaki, S.; Manabe, T.; Hirakami, D. *Analysis of Hydrogen State in Steel and Trapping Using Thermal Desorption Method*. Nippon Steel & Sumitomo Metal Technical Report. 2017, pp. 38–43. Available online: <https://www.nipponsteel.com/en/tech/report/nssmc/pdf/116-08.pdf> (accessed on 18 January 2022).
38. Turk, A.; San Martín, D.; Rivera-Díaz-del-Castillo, P.E.; Galindo-Nava, E.I. Correlation between vanadium carbide size and hydrogen trapping in ferritic steel. *Scr. Mater.* **2018**, *152*, 112–116. [[CrossRef](#)]